Chemical Engineering Journal 428 (2022) 131847

Contents lists available at ScienceDirect

Chemical Engineering Journal

journal homepage: www.elsevier.com/locate/cej

Particle behaviours of biomass gasification in a bubbling fluidized bed

Dali Kong [a], Kun Luo [a,*], Shuai Wang [a,b], Jiahui Yu [a], Jianren Fan [a]

[a] State Key Laboratory of Clean Energy Utilization, Zhejiang University, Hangzhou 310027, PR China
[b] School of Chemical Engineering, University of New South Wales, Sydney, NSW 2052, Australia

ARTICLE INFO

Keywords:
CFD-DEM
Heat and mass transfer
Biomass gasification
Mixing and dispersion

ABSTRACT

Biomass gasification in a bubbling fluidized bed (BFB) reactor is numerically studied based on a particle-scale computational fluid dynamics-discrete element method (CFD-DEM), with thermochemical and polydispersity effects featuring. After model validation, the particle-scale information (e.g., particle motions, particle mixing, solid dispersion, and heat transfer contribution) are thoroughly explored with the discussion of the effects of several critical operating parameters on particle behaviours. The results show that the middle dense region has the highest biomass pyrolysis reaction rate due to the vigorous particle motion. Sand and biomass particles show synchronous horizontal motions, and the solid vertical dispersion coefficients are much higher than the solid horizontal ones, denoting that the vertically introduced gas flow dominates bed hydrodynamics. A higher operating temperature causes a higher solid dispersion coefficient. Elevating temperature and steam to biomass ratio (S/B) first increases and then decreases the particle mixing index. Convection plays a dominant role during the biomass gasification process, followed by the radiation and heat of reaction. The conduction accounts for the smallest proportion and can be neglected. Increasing operating temperature promotes chemical reactions, biomass temperature, and all heat transfer modes. Increasing S/B promotes biomass motions and gasification reactions, leading to more heat consumed and biomass temperature decrease. Decreasing biomass temperature results in a larger temperature difference between biomass particles and bed material, which enhances the conduction, convection, and radiation.

1. Introduction

Increasing global warming and climate change urge to decrease greenhouse gas emissions. The potential route is to reduce the consumption of fossil fuels and increase the utilization of renewable energy. As one of the renewable fuels, biomass has many advantages, such as wide distribution, high storage, and environmental friendliness [1,2]. Biomass gasification is a promising technology to convert raw biomass material to high-value products. Specifically, biomass reacts with gasification agents (e.g., CO_2, steam) at high temperatures to produce syngas (e.g., H_2, CO, and CH_4) [3]. Biomass gasification routinely takes place in a bubbling fluidized bed (BFB) reactor, which shows excellent contact efficiency, high heat and mass transfer performance, and wide fuel flexibility [4–6]. BFB performance highly depends on bed hydrodynamics. Therefore, it is of great significance to deeply understand the in-furnace phenomena (e.g., multi-phase flow, heat and mass transfer, and chemical reactions) for the design and optimization of BFB reactors. However, high costs and complex thermochemical processes inside the reactor (e.g., particle mixing and collisions, bubble formation and eruption, inter-phase coupling, and homogeneous and heterogeneous reactions) hinder the experimental studies of biomass gasification in the BFB reactor.

As an alternative, computational fluid dynamics (CFD) increasingly becomes a powerful tool to understand chemical engineering processes that involve dense gas–solid reacting flow. The existing CFD methods are generally divided into two categories: The Eulerian-Eulerian method and the Eulerian-Lagrangian method. In the former, both solid and fluid phases are regarded as interpenetrating media. This method can accurately predict gas–solid characteristics in large-scale apparatuses at low computational costs and has been broadly employed to simulate dense gas–solid reacting systems in the past decades [7–9]. However, the Eulerian-Eulerian method is unable to analyze the discrete characteristics of particles (e.g., size distribution, rotation, collision, dispersion, shrinkage), which makes it impossible for researchers to obtain more detailed information at the micro aspect in the dense gas–solid reacting system [10]. The above issue can be overcome by the Eulerian-Lagrangian method, in which the computational fluid dynamics coupled with discrete element method (CFD-DEM) is the most typical one. In this approach, the gas phase is regarded as a continuum and the

* Corresponding author.
E-mail address: zjulk@zju.edu.cn (K. Luo).

https://doi.org/10.1016/j.cej.2021.131847
Received 2 July 2021; Received in revised form 7 August 2021; Accepted 11 August 2021
Available online 17 August 2021
1385-8947/© 2021 Elsevier B.V. All rights reserved.

Nomenclature

$A_{p,i}$	Surface area of particle i, m^2
C_D	Drag coefficient
$C_{p,g}$	Specific heat capacity of gas phase, $J\cdot kg^{-1}\cdot K^{-1}$
$C_{p,i}$	Specific heat capacity of particle i, $J\cdot kg^{-1}\cdot K^{-1}$
D_n	Diffusion coefficient of species n, $kg\cdot m^{-1}\cdot s^{-1}$
d	Thickness of gas layer, m
d_p	Particle diameter, m
$e_{n,ij}$	Normal restitution coefficient
$\mathbf{F}_c$	Contact force exerting on a specific particle, N
$\mathbf{F}_d$	Gas force exerting on a specific particle, N
$\mathbf{F}^n_{ij}$, $\mathbf{F}^t_{ij}$	Normal and tangential contact forces between particle i and j, N
$\mathbf{g}$	Gravitational acceleration, $m\cdot s^{-2}$
$h_{pg,i}$	Convective heat transfer coefficient, $W\cdot m^{-2}\cdot K^{-1}$
$\mathbf{I}_{gm}$	Inter-phase momentum exchange rate, $N\cdot m^{-3}$
I_p	Moment of inertia of a specific particle, $kg\cdot m^2$
k	The number of particles colliding with particle i
$k_{n,ij}$, $k_{t,ij}$	Normal and tangential spring coefficients, $N\cdot m^{-1}$
L	Distance from contact point to particle center, m
l_{ij}	Distance between particle i and j, m
$\mathbf{n}_{ij}$	Normal unit vector between particle i and j
N_p	Particle number
$N_{p,\Omega}$	Particle number in the domain Ω
$Nu_{p,i}$	Nusselt number of particle i
N_x, N_y, N_z	Grid number along x,y, and z directions
P_i	Gas partial pressure of gas specie i, Pa
Pr	Prandtl number
Q_g	Gas flux, Nm^3/hr
Q_{gp}	Gas-particle convective heat transfer rate, $W\cdot m^{-3}$
Q_{pgp}	Particle-gas-particle conductive heat transfer rate, $W\cdot m^{-3}$
Q_{pp}	Particle-particle conductive heat transfer rate, $W\cdot m^{-3}$
Q_{rad}	Radiative heat transfer rate, $W\cdot m^{-3}$
R	Gas constant, J·mol-1·K-1
$R_{c,ij}$	Radius of contact region, m
Re_p	Particle Reynold number
R_{in}, R_{out}	Lower and upper bounds of conductive heat transfer region, m
$R_{p,i}$, $R_{p,j}$	Diameters of particle i and j, m
t	Time instant, s
$\mathbf{t}_{ij}$	Tangential unit vector between particle i and j
T_{env}	Temperature of environment, K
T_g	Temperature of gas phase, K
$T_{g,\Omega}$	Temperature of gas phase in the domain Ω, K
$T_{p,i}$, $T_{p,j}$	Temperatures of particle i and j, K
T_{Rg}	Radiation temperature of gas phase, K
$\mathbf{u}_g$	Velocity vector of gas phase, $m\cdot s^{-1}$
$\mathbf{v}_p$	Velocity vector of particle i, $m\cdot s^{-1}$
V_c	Volume of computational cell, m^3
V_i	Volume of particle i, m^3
X_n	Mass fraction of nth species

Greek symbols

ε_g	Void fraction
$e_{p,i}$	Emissivity of particle i
β	Inter-phase momentum exchange coefficient, $kg\cdot m^{-3}\cdot s^{-1}$
ΔH_{rg}	Heat source of gas phase due to chemical reaction, $W\cdot m^{-3}$
ΔH_{rs}	Heat source of solid phase due to chemical reaction, $W\cdot m^{-3}$
κ_g	Gas thermal conductivity, $W\cdot m^{-1}\cdot K^{-1}$
$\kappa_{p,i}$, $\kappa_{p,j}$	Thermal conductivity of particle i and j, $W\cdot m^{-1}\cdot K^{-1}$
γ_{Rg}	Radiative heat transfer coefficient of gas phase, $W\cdot m^{-2}\cdot K^{-4}$
$\eta_{n,ij}$, $\eta_{t,ij}$	Normal and tangential damping coefficients, $kg\cdot s^{-1}$
$\delta_{n,ij}$, $\delta_{t,ij}$	Normal and tangential overlap displacements, m
μ	Friction coefficient
μ_g	Gas viscosity, $kg\cdot m^{-1}\cdot s^{-1}$
ρ_g, ρ_p	Gas and particle density, $kg\cdot m^{-3}$
$\boldsymbol{\omega}_p$	Particle angular velocity, s^{-1}

Subscripts

g	Gas phase
i	Particle i
ij	Interactions between particle i and j
j	Particle j
n	Variables in normal direction
p	Properties of particle

Acronyms

BFB	Bubbling fluidized bed
CFD	Computational fluid dynamics
DEM	Discrete element method
FVM	Finite volume method
LSD	Linear spring dashpot
MFIX	Multiphase Flow with Interphase Exchange
S/B	Steam to biomass ratio
3D	Three-dimensional

particles are treated as a discrete phase. Each particle is tracked independently and has its discrete properties (e.g., size, temperature, composition, density, and velocity). The CFD-DEM approach can thus provide detailed information at the particle-scale level, such as the inter-particle/phase interactions, heat transfer mechanism, and reaction characteristics.

Recently, many researchers have employed the CFD-DEM approach to explore biomass gasification in fluidized bed reactors [11–13]. Yang et al. [14] simulated the biomass gasification process in a BFB and found that the single side fuel inlet led to the asymmetrical distributions of gas–solid flow and product yields. Increasing temperature, steam/biomass ratio, and equivalence ratio performed a positive effect on bed voidage, forces, and solid dispersion. Wang et al. [15] studied the biomass gasification process in a lab-scale BFB reactor and observed that biomass particles tended to migrate and aggregate to the bed surface during the gasification process. Heterogeneous reactions mainly occurred at the bed surface while homogeneous reactions commonly took place in the freeboard. Ku et al. [16] compared gasification performance between raw and torrefied biomass in an air-blown fluidized-bed gasifier and claimed that the torrefied biomass needed a longer conversion process. Besides, raising the fuel feed location decreased the total gas yield and carbon conversion. Ostermeier et al. [17] employed a coarse-grain CFD-DEM approach to study the biomass gasification process in a fluidized bed reactor and demonstrated that the pressure drop, gas composition, and conversion time agreed well with the experimental data. Wang et al. [18] developed a high-fidelity CFD-DEM approach to investigate biomass gasification in a BFB and tested the sensitivity of contact and drag models on thermochemical results. They proved that the computational efficiency using a linear spring-dashpot (LSD) contact model is 6.8 times that using a non-linear Hertzian contact model. The drag models played a crucial role in hydrodynamics and had an insignificant effect on the thermochemical results. However, the above studies only focus on macroscopic information (e.g., flow patterns, syngas yield, pressure drop, carbon conversion, and gas composition), while particle behaviours on the micro-scale (e.g., particle mixing, heat and mass transfer, solid dispersion) during the biomass gasification process are not reported, which limits the fundamental understanding of gas–solid flow characteristics and thermochemical properties [19].

To fulfil this gap, a numerical model using CFD-DEM coupled with thermochemical and polydispersity sub-models is built to study gas–solid hydrodynamics, and heat and mass transfer behaviours during the biomass gasification process in a BFB reactor. In this work, a reactive CFD-DEM approach featuring polydispersity and thermochemical sub-models is developed to study biomass gasification process in a BFB reactor at the particle-scale level. The detailed particle-scale investigation of the biomass particles will provide a more in-depth understanding of the gasification process, concerning the effect of chemical reactions, and the comparison of the biomass and sand particles. The article is organized as follows: Section 2 details the mathematical model. Section 4.2 summarizes the flow patterns, trajectories of biomass and sand particles, particle temperature distribution. Section 4.3 explores the mixing and dispersion of particles together with the discussion of the effects of operating parameters. Section 4.4 analyses the contribution of different heat transfer modes for biomass particles and the performance of four heat transfer modes under different operating parameters. Section 4.5 gives the distribution of product gas concentration and reaction rates, as well as the corresponding relationship between them. The conclusion is drawn in Section 5.

2. Numerical methods

2.1. Governing equations for gas–solid phases

The gas phase is treated as a continuum and is governed by the following conservation equations. The continuity equation is given by:

$$\frac{\partial(\varepsilon_g\rho_g)}{\partial t}+\nabla\left(\varepsilon_g\rho_g\mathbf{u}_g\right)=\delta\dot{m}_p \tag{1}$$

where ε_g denotes the voidage, ρ_g is the gas density, $\mathbf{u}_g$ is the gas velocity vector, $\delta\dot{m}_p$ represents the volumetric consumption or generation rate of gas species due to heterogeneous reactions.

The momentum equation is given by:

$$\frac{\partial\left(\varepsilon_g\rho_g\boldsymbol{u}_g\right)}{\partial t}+\nabla\left(\varepsilon_g\rho_g\boldsymbol{u}_g\boldsymbol{u}_g\right)=\nabla\left(\varepsilon_g\tau_g\right)-\varepsilon_g\nabla p_g\ +\ \rho_g\varepsilon_g\mathbf{g}-\sum_{m=1}^{M}\mathbf{I}_{gm} \tag{2}$$

where p_g is the gas pressure, $\mathbf{g}$ is the gravitational acceleration, τ_g is the gas phase stress tensor. The momentum exchange term between gas phase and m^{th} solid phase ($\mathbf{I}_{gm}$) is defined as:

$$\begin{aligned}\mathbf{I}_{gm}&=\frac{1}{V_c}\sum_{i=1}^{N_p}\mathbf{F}_d\\&=\frac{1}{V_c}\sum_{i=1}^{N_p}\left(-\nabla P_g(x_i)V_i+\frac{\beta V_i}{(1-\varepsilon_g)}\left(\mathbf{u}_g(x_i)-\mathbf{v}_p\right)\right)\end{aligned} \tag{3}$$

where N_P is the total number of particles, $\mathbf{F}_d$ is the force exerted on a single particle by the gas phase. V_c and V_i represent the volume of the grid cell and particle, respectively. β denotes the drag coefficient. $\mathbf{v}_p$ is the particle translational velocity. Further details about the governing equations can refer to the literature [18,20].

The species conservation equation is given by:

$$\frac{\partial(\varepsilon_g\rho_gX_i)}{\partial t}+\nabla\cdot\left(\varepsilon_g\rho_g\mathbf{u}_gX_i\right)=\nabla\cdot\left(\varepsilon_g\rho_gD_n\nabla X_i\right)+R_{gi} \tag{4}$$

where X_i and D_i represent the mass fraction and diffusivity coefficient of ith gas species, respectively. R_{gi} is the mass source term due to homogeneous reactions.

The energy conservation equation:

$$\frac{\partial\left(\varepsilon_g\rho_gC_{pg}T_g\right)}{\partial t}+\nabla\left(\varepsilon_g\rho_g\mathbf{u}_gC_{pg}T_g\right)=\nabla\cdot\left(\varepsilon_g\kappa_g\nabla T_g\right)+Q_{gp}-\Delta H_{rg}+\gamma_{Rg}\left(T_{Rg}^4-T_g^4\right) \tag{5}$$

where the terms on the right-hand side denote the volumetric heat flux due to conduction, convection, reaction, and radiation, respectively. T_g and T_{Rg} denote the gas temperature and the gas phase radiation temperature, respectively. γ_{Rg} is the radiative heat transfer coefficient, C_{pg} and κ_g are the specific heat capacity and thermal conductivity of the gas phase, respectively.

The motion of particles obeys Newton's law of motion. The governing equations of the particle phase are as follows [21]:

$$m_p\frac{d\mathbf{v}_p}{dt}=m_p\mathbf{g}+\mathbf{F}_d+\mathbf{F}_c \tag{6}$$

$$I_p\frac{d\omega_p}{dt}=\sum_{j=1,j\neq i}^{k}\left(L\mathbf{n}\times\mathbf{F}_{ij}^t\right) \tag{7}$$

where m_p is particle mass. I_p is the particle momentum of inertia. $\boldsymbol{\omega}_p$ is the particle rotational velocity. k is the total number of particles that collide with particle i. L is the distance between the contact point and the particle centroid. $\mathbf{F}_c$ is the contact force due to particle–particle/wall collisions, which includes normal and tangential components [22]:

$$\mathbf{F}_c=\sum_{j=1,j\neq i}^{k}\left(\mathbf{F}_{ij}^n+\mathbf{F}_{ij}^t\right) \tag{8}$$

$$\mathrm{F}_{ij}^n=-\left(k_{n,ij}\delta_{n,ij}-\eta_{n,ij}\dot{\delta}_{n,ij}\right)\mathrm{n}_{\mathrm{ij}} \tag{9}$$

$$\mathbf{F}_{ij}^t=\begin{cases}-\left(k_{t,ij}\delta_{t,ij}-\eta_{t,ij}\dot{\delta}_{t,ij}\right)\mathbf{t}_{ij}, & \left|\mathbf{F}_{ij}^t\right|\leqslant\mu\left|\mathbf{F}_{ij}^n\right|\\ -\mu\left|\mathbf{F}_{ij}^n\right|\mathbf{t}_{ij}, & \left|\mathbf{F}_{ij}^t\right|>\mu\left|\mathbf{F}_{ij}^n\right|\end{cases} \tag{10}$$

Wang et al. [18] proved that using LSD model will speed up the calculation without affecting the accuracy of prediction results. Therefore, the linear spring-dashpot (LSD) model is employed to calculate the variables related to the particle properties (e.g., spring stiffness k, damping coefficient η, friction coefficient μ) [23] in this work.

The energy conservation equation of particle is defined as:

$$m_pC_{p,i}\frac{dT_{p,i}}{dt}=Q_{gp,i}+Q_{pp,i}+Q_{pgp,i}\ +\ Q_{rad,i}-\Delta H_{rs} \tag{11}$$

where $C_{p,i}$ and $T_{p,i}$ are the specific heat capacity and particle temperature of particle i, respectively. $Q_{pp,i}$ and $Q_{pgp,i}$ are the heat flux through particle–particle and particle-gas-particle conduction. $Q_{gp,i}$, $Q_{rad,i}$, and ΔH_{rs} are the heat flux via convection, radiation, and reaction [18].

The particle–particle conduction is given by [24]:

$$Q_{pp,ij}=4\frac{\kappa_{p,i}\kappa_{p,j}}{\kappa_{p,i}+\kappa_{p,j}}R_{c,ij}\left(T_{p,j}-T_{p,i}\right) \tag{12}$$

$$R_{c,ij}=\sqrt{R_{p,j}^2-\left(\frac{R_{p,j}^2-R_{p,i}^2+l_{ij}^2}{2l_{ij}}\right)^2} \tag{13}$$

where κ_p is the particle thermal conductivity, $R_{c,ij}$ is the radius of the contact surface, R_p is particle radius, l_{ij} is the distance between the centre of two colliding particles.

The particle-gas-particle heat transfer mode is realized by a thin gas layer (i.e., $0.2d_p$ by default) surrounding particle, and this mode is activated when the gas layers of two particles contact. The particle-gas-particle mode is given by [18]:

$$Q_{pgp,ij} = \kappa_g\left(T_{p,j} - T_{p,i}\right)\int_{R_{in}}^{R_{out}} \frac{2\pi r}{l_{ij} - \left(\sqrt{R_{p,i}^2 - r^2} + \sqrt{R_{p,j}^2 - r^2}\right)} dr \tag{14}$$

$$R_{in} = \begin{cases} 0, & l_{ij} > \left(R_{p,i} + R_{p,j}\right) \\ \sqrt{R_{p,j}^2 - \left(\frac{R_{p,j}^2 - R_{p,i}^2 + l_{ij}^2}{2l_{ij}}\right)^2}, & l_{ij} \leqslant \left(R_{p,i} + R_{p,j}\right) \end{cases} \tag{15}$$

$$R_{out} = \sqrt{\left(R_{p,j} + d\right)^2 - \left(\frac{\left(R_{p,j} + d\right)^2 - R_{p,i} + l_{ij}^2}{2l_{ij}}\right)^2} \tag{16}$$

where d is the thickness of the gas layer. R_{in} and R_{out} are the lower bound and upper bound of the contact region.

The particle-gas convection is given by:

$$Q_{gp,i} = h_{pg,i}A_{p,i}\left(T_g - T_{p,i}\right) \tag{17}$$

$$h_{pg,i} = \frac{\mathrm{Nu_{p,i}d_{p,i}}}{\kappa_g} \tag{18}$$

$$\mathrm{Nu_{p,i}} = 2.0 + 0.6Re_{\mathrm{p,i}}^{1/2}Pr^{1/3} \tag{19}$$

$$Pr = \mu_g C_{p,g}/\kappa_g \tag{20}$$

where $h_{pg,i}$ is heat transfer coefficient, $A_{p,i}$ is particle surface area, $\mathrm{Nu}_{p,i}$ is the particle Nusselt number, Pr is the Prandtl number.

The particle–particle radiation is given by:

$$Q_{rad,i} = e_{p,i}A_{p,i}\sigma\left(T_{env}^4 - T_{p,i}^4\right) \tag{21}$$

$$T_{env} = \varepsilon_g T_{g,\Omega} + \left(1 - \varepsilon_g\right)\frac{1}{N_{p,\Omega}}\sum_{j=1,j\neq i}^{N_{p,\Omega}} T_j \tag{22}$$

where $e_{p,i}$ is particle emissivity, σ is the Stefan-Boltzmann constant, T_{env} is a combination of gas temperature and the average particle temperature in a region Ω. $N_{p,\Omega}$ is the total number of particles in the region Ω.

2.2. Drag model

Drag force plays an important role in simulating dense gas–solid flow in BFB. During the biomass gasification process, the properties of biomass particles (e.g., particle mass, particle size) will change with the progress of chemical reactions. In this work, the shrinking core model is adopted [25,26], in which the particle density remains constant while the particle size is reduced as the particle mass changes:

$$d_p = \sqrt[3]{\frac{6m_p}{\pi\rho_p}} \tag{23}$$

The variation of particle mass caused by chemical reactions leading to great disparities in the particle size distribution. In a polydispersed system, the traditional drag models that developed based on homogeneous systems [27,28] tended to underestimate the drag force for large-size particles and overestimated the drag force for small-size particles [29]. Therefore, the drag model with the polydispersity effect considered is employed in this work [29,30]:

$$\beta = \frac{18\mu_g\varepsilon_g(1 - \varepsilon_g)}{d_{p,i}^2}F_i \tag{24}$$

$$F_i = \left(\varepsilon_g y_i + (1 - \varepsilon_g)y_i^2 + 0.064\varepsilon_g y_i^3\right)F \tag{25}$$

Table 1
Proximate analysis and ultimate analysis of biomass.

Ultimate analysis (wt%, d. a. f. basis)				Proximate analysis (wt%, as-received basis)			
C (d. a. f.)	H (d. a. f.)	O (d. a. f.)	N&S (d. a. f.)	Moisture	Ash	Volatile	Fixed Carbon
46.29	6.48	46.08	1.15	11.89	1.56	71.78	14.77

$$F = \frac{10\left(1 - \varepsilon_g\right)}{\varepsilon_g^2} + \varepsilon_g^2\left(1 + 1.5\left(1 - \varepsilon_g\right)^{0.5}\right) + \frac{0.413Re_p}{24\varepsilon_g^2}\left[\frac{\varepsilon_g^{-1} + 3\varepsilon_g\left(1 - \varepsilon_g\right) + 8.4Re_p^{-0.343}}{1 + 10^{3\left(1-\varepsilon_g\right)}Re_p^{-0.5-2\left(1-\varepsilon_g\right)}}\right] \tag{26}$$

$$y_i = \frac{d_{p,i}}{d_p} \tag{27}$$

$$d_p = \frac{\sum_{i=1}^{c} N_i d_{p,i}^3}{\sum_{i=1}^{c} N_i d_{p,i}^2} \tag{28}$$

$$\mathrm{Re_p} = \frac{\rho_g\varepsilon_g\left|\mathbf{u}_g - \mathbf{v}_p\right|\mathrm{d_p}}{\mu_g} \tag{29}$$

where c is the total number of particles in the system, $d_{p,i}$ is the diameter of particle i, N_i is the number of particles with the same size as particle i.

2.3. Reaction kinetics

The biomass material used in this work is pine wood, which is consistent with the experiment [3]. The proximate analysis and ultimate analysis of the biomass are listed in Table 1.

After feeding into the reactor, biomass particles are heated rapidly and pyrolyzed. The volatile is released from the biomass particles and then char conversion occurs. In this work, the pyrolysis of biomass is described as follows:

$$\begin{aligned} &\mathrm{Biomass} \rightarrow \alpha_1\mathrm{CO} + \alpha_2\mathrm{CO_2} + \alpha_3\mathrm{CH_4} + \alpha_4\mathrm{H_2} + \alpha_5\mathrm{H_2O} \\ &+ \alpha_6\mathrm{Char} + \alpha_7\mathrm{ash}, \ \sum_i \alpha_i = 1 \end{aligned} \tag{30}$$

where the coefficient of each product in the equation is calculated based on the proximate analysis and ultimate analysis of the biomass material

Table 2
Chemical reaction and reaction rates.

Chemical reaction equation	Chemical reaction rate
Heterogeneous reactions:	
R1: $C + H_2O \rightarrow CO + H_2$	$r_1 = A_p p_{H_2O}\frac{r_{diff,1}r_{kin,1}}{r_{diff,1} + r_{kin,1}}$
	$r_{kin,1} = 45.6T_p\exp(\frac{4.37 \times 10^7}{RT_p})$
	$r_{diff,1} = 5 \times 10^{-12}(\frac{T_g + T_p}{2})^{0.75}/d_p$
R2: $C + CO_2 \rightarrow 2CO$	$r_2 = A_p p_{CO_2}\frac{r_{diff,2}r_{kin,2}}{r_{diff,2} + r_{kin,2}}$
	$r_{kin,2} = 8.3T_p\exp(\frac{4.37 \times 10^7}{RT_p})$
	$r_{diff,2} = 5 \times 10^{-12}(\frac{T_g + T_p}{2})^{0.75}/d_p$
Homogeneous reactions:	
R3: $CH_4 + H_2O \rightarrow CO + 3H_2$	$r_3 = 3 \times 10^8\exp(-1.26 \times 10^8/RT_g)[CH_4][H_2O]$
R4: $CO + H_2O \leftrightarrow CO_2 + H_2$	$r_{4f} = 2.78 \times 10^3\exp(-1.26 \times 10^7/RT_g)[CO][H_2O]$
	$r_{4b} = 9.59 \times 10^4\exp(-4.66 \times 10^7/RT_g)[CO_2][H_2]$
	$r_{eq} = 0.029\exp(3.40 \times 10^7/RT_g)$
	$r4 = (r4f - r4b)/req$

Table 3
Operating parameters and thermophysical properties.

Parameters	Value	Unit
Bed size (x, y, z)	230 × 1500 × 4.5	mm
Cell Number (N_x, N_y, N_z)	46, 200, 1	–
Operating temperature	1043, 1093, 1143, 1193	K
Particle diameter (Sand/Biomass)	1.5/1.5	mm
Particle density (Sand/Biomass)	2600/470	$kg{\cdot}m^{-3}$
Particle temperature (Biomass)	300	K
Particle specific heat (Sand/Biomass)	860/1500	$J{\cdot}kg^{-1}{\cdot}K^{-1}$
Particle thermal conductivity (Sand/Biomass)	0.03/0.04	$W{\cdot}m^{-1}{\cdot}K^{-1}$
Particle emissivity (Sand/Biomass)	0.7/0.7	–
Particle spring stiffness (Sand/Biomass)	1000/1000	$N{\cdot}m^{-1}$
Particle restitution coefficient (Sand/Biomass)	0.9/0.9	–
Particle friction coefficient (Sand/Biomass)	0.3/0.3	–
Biomass feed rate	0.3125	g/s
Inlet gas flow rate	1.8395	g/s

[3]. The elements such as N, S, and Cl are neglected in the present model due to their minor amounts, and hydrocarbons are represented by CH_4. The above assumptions have been widely applied in the simulation of biomass gasification [1,25,31].

A single step first-order Arrhenius reaction rate is employed to describe the pyrolysis process [32,33]:

$$\frac{dm_{volatiles}}{dt} = -5\times10^{6}exp(-\frac{1.2\times10^{8}}{RT_p})m_{volatiles} \tag{31}$$

where $m_{volatiles}$ is the mass of volatiles in the biomass particle, R is gas constant, T_p is particle temperature. After pyrolysis, the char remaining in the biomass particle reacts with H_2O and CO_2 to generate CO and H_2. In addition to the heterogeneous reactions related to char gasification, there are also homogeneous reactions in the reactor, including the water–gas shift reaction and the methane gasification reaction. The char conversion reactions and the corresponding reaction rates are summarized in Table 2 [34–37].

For heterogeneous reactions, the kinetic rate r_{kin} and the diffusion rate r_{diff} are considered. A_p is the particle surface area. P_i is the gas partial pressure. For homogeneous reactions, the reaction rate is proportional to the reactant concentration and the kinetic rate constant.

3. Model setup

The investigated object is a lab-scale BFB reactor, which is taken from the experimental test rig [3]. The height, width, and thickness of the BFB are 1500 mm, 230 mm, 4.5 mm, respectively. The grids with 46, 200, and 1 in X, Y, and Z directions are allocated, respectively. The grid size ranges from 4.5 mm to 7.5 mm, 3–5 times the particle diameter, which meets the requirement of typical CFD-DEM simulations [38]. A quasi-3D model is adopted to balance numerical accuracy and calculation efficiency. The thickness of the BFB is three times the particle diameter. It is well accepted that the computational efficiency of the CFD-DEM simulation is limited by tracking each particle and resolving the inter-particle collisions. A fully 3D computational domain is inevitable to increase the number of particles in the computational domain and the consumption of computational resources. Moreover, the quasi-3D model has been proved to be reasonable to simulate gas–solid hydrodynamics [6,15,39].

The thermochemical sub-models are implemented on the open-source software MFIX, which has been verified to be able to simulate gas–solid flow with high accuracy and robustness [40,41]. At each fluid time step, the particle phase and the gas phase are coupled explicitly by the interphase source term, and the particle properties (e.g., mass, diameter, temperature) are updated. For the gas phase, the governing equations are discretized based on the finite volume method (FVM). The

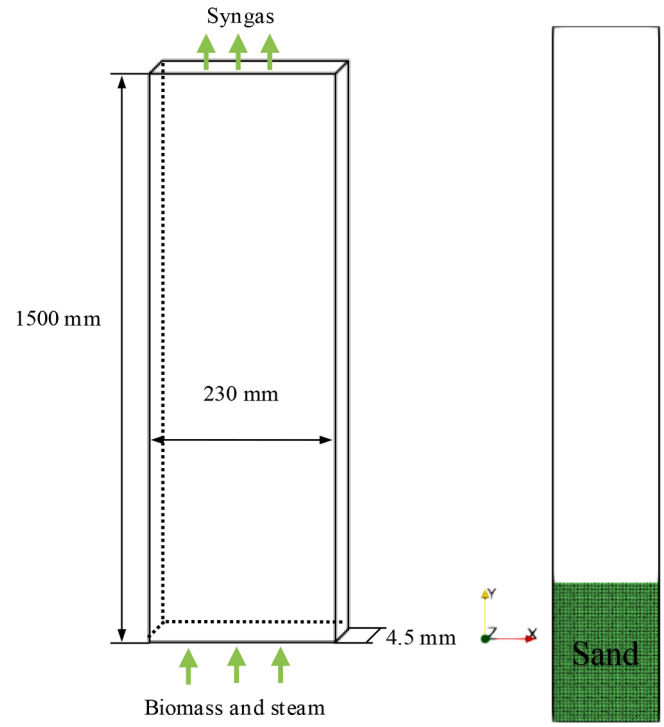

Fig. 1. The schematic diagram of the investigated BFB reactor.

SIMPLE algorithm is employed to model the coupling between the gas velocity and gas pressure. The simulation runs on the supercomputer platform at Zhejiang University. For each case, 32 CPU processors based on Distributed Memory Parallel (DPM) are adopted to accelerate computational speed. The physical time for each case is 20s, which takes about 14 days to complete. The gas time step is 1×10^{-5} s while the solid time step is specified as 1/50 of the minimum collision time.

Operating parameters, boundary conditions, and particle properties (e.g., thermal conductivity, specific heat, emissivity) are summarized in Table 3. The bed material particles are initially packed in the lower part of the BFB with a height of 350 mm. Biomass particles, steam, and nitrogen enter the reactor from the bottom. The pressure at the outlet is set as 101325 Pa, and the walls are assigned as no-slip and constant temperature boundary conditions. The case with an operating temperature of 1093 K and steam to biomass ratio (S/B) of 0.8 is employed as the base case. Thermophysical properties are calculated based on the thermal databases [42,43]. In the biomass gasification process, operating temperature and steam to biomass ratio (S/B) are two critical factors that significantly affect gasification performance [1,15,44]. In this study, four sets of operating temperature (i.e., 1043 K, 1093 K, 1143 K, and 1193 K) and four sets of S/B (i.e., 0.6, 0.8, 1.0, and 1.2) are set to study the effects of temperature and S/B on micro-scale particle behaviours and biomass gasification performance. The value of S/B keeps constant at 0.8 when the temperature changes and the temperature keeps constant at 1093 K when S/B changes.

4. Result and discussion

4.1. Model validation

The CFD-DEM approach has been systematically and comprehensively verified on hydrodynamics and heat transfer aspects in our previous publications [45,46], which is outlined here for completeness. Specifically, Wang et al. [45] validated the CFD-DEM approach with the experimental data regarding a particle cooling process in a fluidized bed. The gas flows with an initial temperature of 20 °C is introduced from the bed bottom to fluidize and cool particles with an initial temperature of

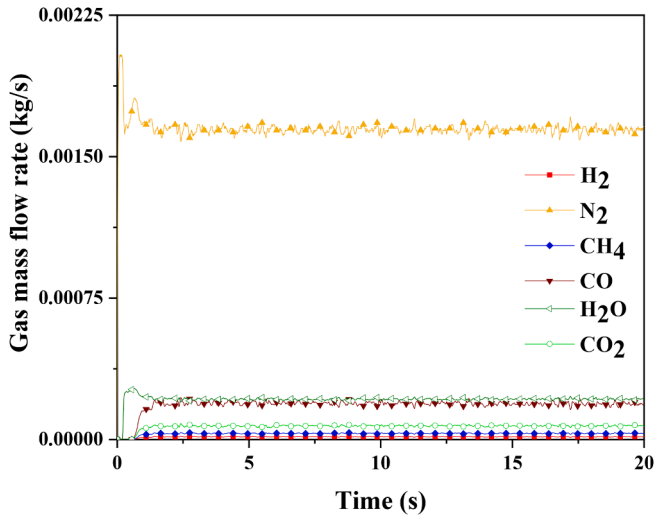

Fig. 2. The time-evolution profiles of mass flow rates of gas species at the outlet of the BFB.

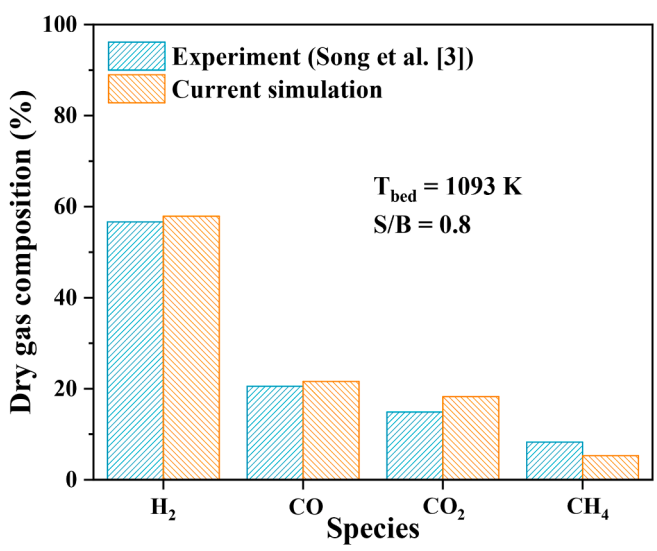

Fig. 3. Comparison between simulation results and experimental data [3].

90 °C. The solid holdup and solid volume flux (a combination of solid holdup and solid velocity) of simulation results and experimental data [47] show good agreement, and the "core-annulus" structure is successfully captured (see Fig. S1 of Supporting Information). Besides, the time-evolution profiles of particle-averaged temperature under different operating parameters predicted by the simulation are consistent with that observed in the experiment (see Fig. S2 of Supporting Information). The above validations prove the reasonability of the CFD-DEM approach in predicting bed hydrodynamics and heat transfer characteristics in fluidized beds (see Fig. 1).

After the validation of hydrodynamics and heat transfer, the chemical reaction model is also validated. The time-evolution profiles of instantaneous mass flow rates of gas species at the BFB exit are shown in Fig. 2. The mass flow rate of gas specie *i* through a surface is computed by summing the product of volume fraction, density of gas specie *i*, gas velocity normal to the facet in cell *j*, and the facet area. As the fluidized gas enters the BFB from the bottom distributor, N_2 is first blown away from the outlet, followed by H_2O. As chemical reactions march, the other four gas species (i.e., H_2, CH_4, CO, CO_2) escape the outlet at about 0.6s. At about 5s, the mass flow rates of all gas species tend to be stable with time, indicating that the system reaches a dynamic equilibrium

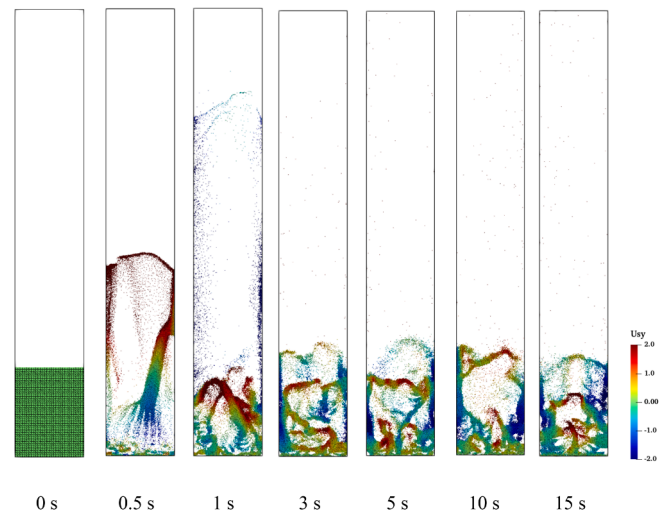

Fig. 4. Time-evolution flow patterns in the BFB (coloured by Y-direction velocity).

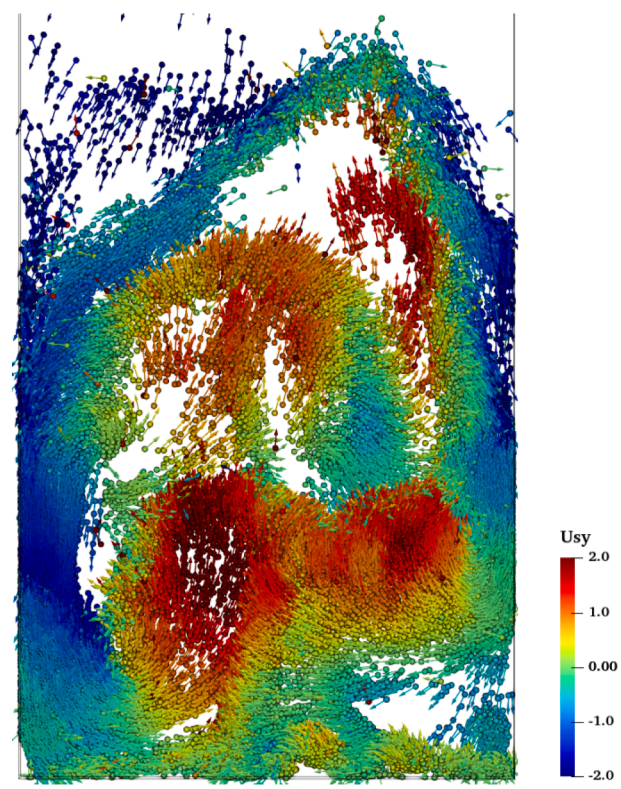

Fig. 5. Instantaneous flow pattern in the BFB (coloured by Y-direction velocity).

state. Therefore, the data after 5s are adopted as statistical samples to calculate the time-averaged results and void the startup effect.

As shown in Fig. 3, the predicted results of H_2 and CO agree well with the experimental data [3], while that of CO_2 and CH_4 show slight discrepancies. In the biomass gasification process, there are hundreds of homogeneous and heterogeneous reactions (e.g., drying, pyrolysis, and gasification), and it is impractical to implement such complex reactions in the model. Thus, the chemical reactions are simplified into several global reactions. In addition, reaction kinetics play a key role in chemical reactions, which have varied values according to different literature [34,44,48]. The discrepancies between the numerical results and

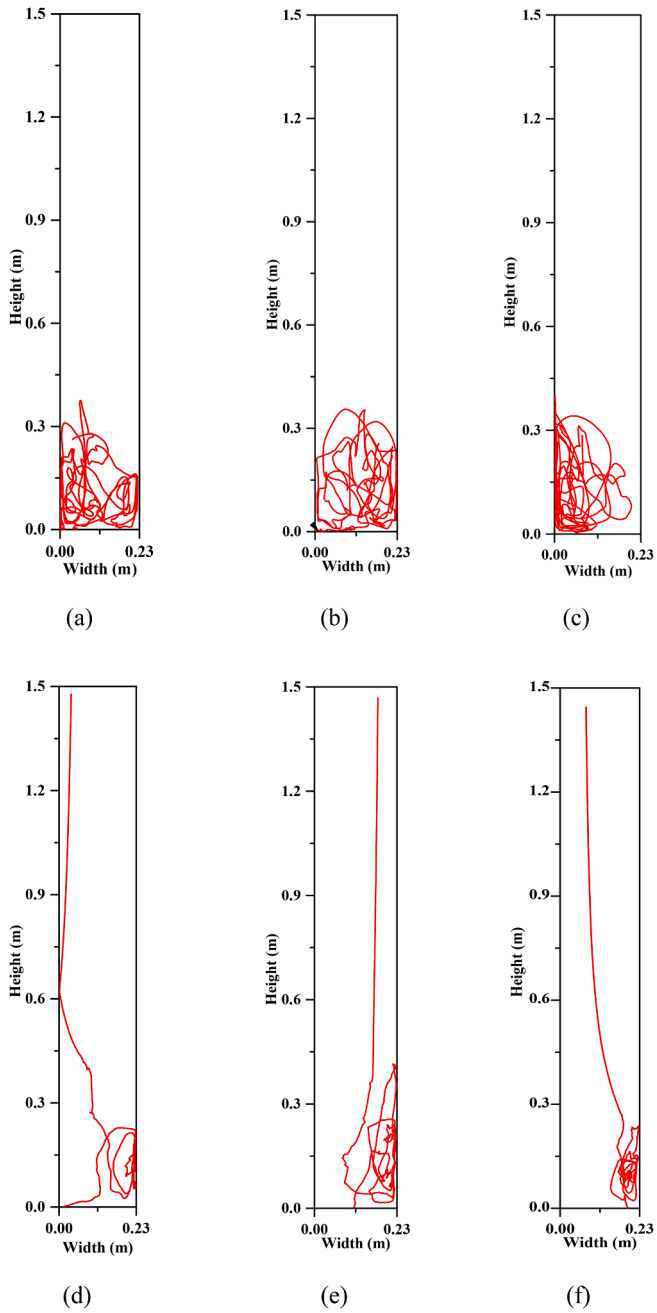

Fig. 6. Particle trajectories of particles: (a-c): sand particles; (d-f): biomass particles.

experimental data are inevitable but acceptable. Hence, the present model can reliably predict the thermochemical properties of the biomass gasification process in BFB reactors.

4.2. General flow pattern

Time-evolution flow patterns in the BFB during the biomass gasification process are shown in Fig. 4. At the initial time, the sand particles are packed in the lower part of the bed. As the gas flow enters the bed from the bottom, an obvious start-up process is observed. At 0.5s, bed expansion together with large-size bubbles occurs attributed to the introduced gas flow, which carries a large number of particles upwards. At 1s, the bubbles burst at the bed surface, and many particles fall along the wall. At the same time, new bubbles are formed in the lower part of the bed. After 3s, the bed height is maintained at a stable value, indicating that the flow patterns in the bed reach a stable state. Bubbles constantly form, rise, and burst in the BFB, which plays a key role in shaping flow patterns.

Fig. 5 shows the instantaneous flow pattern in the BFB after the equilibrium state of the system is achieved. In the X direction, most particles in the middle region rise with positive velocities, while the particles in the near-wall region fall with negative velocities. The particles in the middle region are entrained by bubbles and rise until the bubble eruption, and then the particles are scattered in the freeboard region. In addition, due to the influence of bubble behaviours, the particle concentration in the near-wall region is significantly higher than that in the middle region. At the bottom of the BFB, particles tend to move to the middle region and then be carried upwards by bubbles. The typical behaviours of bubbles and particles improve the mixing property and the resulting heat and mass transfer performance.

Fig. 6 shows the trajectories of three typical sand and biomass particles. For the sand particles, the maximum height is usually less than 0.5 m. Due to the particle–particle/gas interactions, sand particles move irregularly in the dense phase region. After entering the bed, biomass particles are entrained by particle stream to move towards the middle region and then collide with other particles. During the gasification process, the size and mass of biomass particles are reduced. Finally, these biomass particles with small size and mass are carried by the gas flow to the upper part of the bed and finally escape from the reactor.

Fig. 7 gives the instantaneous distribution of particle temperature and time-evolution profile of particle-averaged temperature of biomass particles in the BFB. The particle-averaged biomass particle temperature ($T_{bio,\ avg}$) is formulated as:

$$T_{bio,avg} = \frac{1}{N_{p,bio}} \sum_{i=1}^{N_{p,bio}} T_{i,bio} \tag{32}$$

where $N_{p,\ bio}$ is the total number of biomass particles in the bed at this time, $T_{i,\ bio}$ is the temperature of biomass particle i.

As shown in the figure, the particles with low temperatures are distributed in the bottom region and reside in the bed for a short time. The biomass particles with low temperatures enter the bed from the bottom and quickly mix with the bed material due to the intense gas–solid momentum exchange, resulting in significant heat and mass transfer. In this process, the temperature of biomass particles increases sharply and reaches a stable state at about 5s. The temperature variation trend is consistent with that of the CFD-DEM simulations as reported by Li et al [13].

Fig. 8 illustrates the particle-averaged temperature of biomass particles in the whole bed after the system reaches the equilibrium state under different operating temperatures and S/B. A higher operating temperature leads to a larger temperature difference between biomass particles and gas/sand particles in the BFB, which leads to more intense heat exchange. Therefore, increasing operating temperature increases biomass particle temperature. Higher S/B promotes endothermic chemical reactions and the heat consumed during the reaction process. Therefore, the temperature of biomass particles decreases with the increase of S/B.

4.3. Mixing and dispersion

In the BFB, the heat and mass transfer of particles are closely related to particle behaviours. Hu et al. [49] found that there would be hot spots in the fluidized bed, which was caused by uneven particle mixing and would seriously affect reactor performance. Therefore, the particle motions and mixing must be deeply studied. A uniform and controllable particle mixing process can improve the heat and mass transfer efficiency, thus improving the overall system performance [6]. In this work, the Lacey mixing index (MI) [50] is adopted to evaluate the particle mixing process, which is defined as:

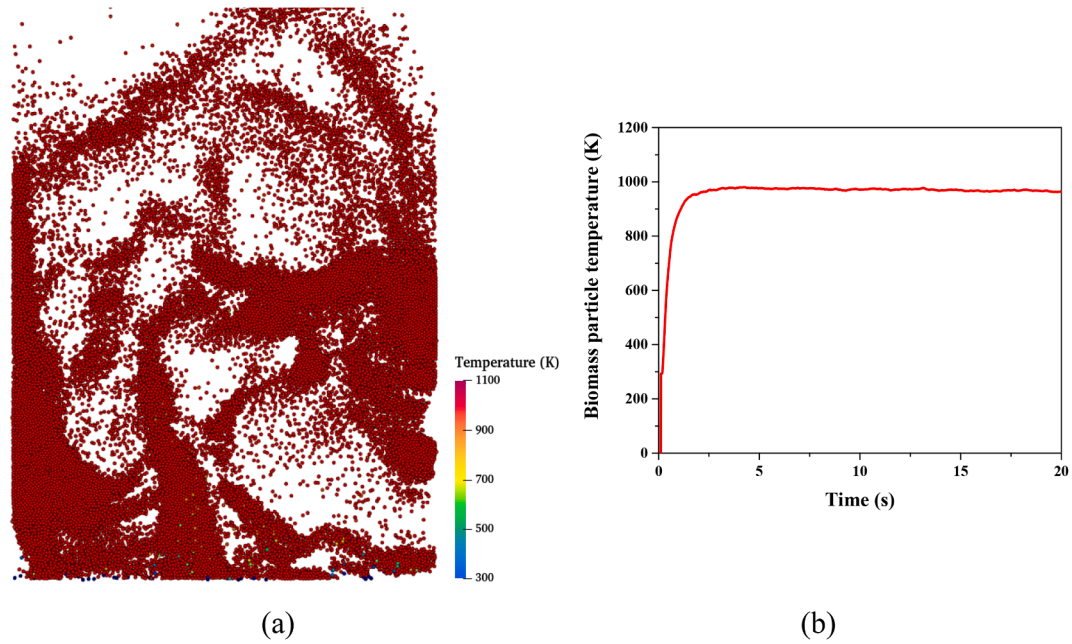

Fig. 7. Instantaneous distribution of particle temperature (a) and time-evolution of particle-averaged biomass particle temperature in the BFB (b).

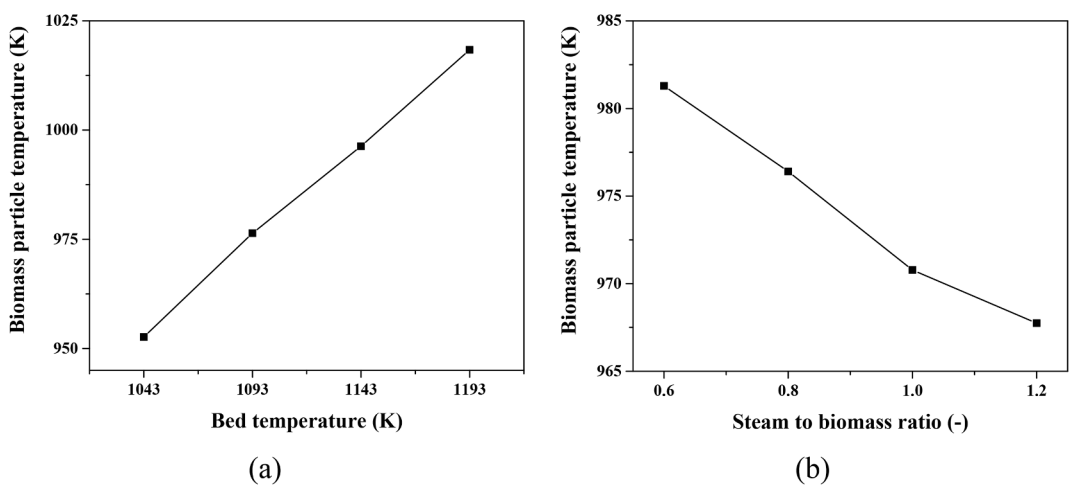

Fig. 8. Particle-averaged biomass particle temperature under different operating temperatures (a) and S/B (b).

$$\mathrm{MI} = \frac{\sigma_0^2 - S^2}{\sigma_0^2 - \sigma_r^2} \tag{33}$$

$$\sigma_0^2 = \bar{c}(1-\bar{c})\sigma_r^2 = \bar{c}(1-\bar{c})/\bar{n}S = \sqrt{\frac{1}{N-1}\sum_{i=1}^{N}(\bar{c}-c_i)^2} \tag{34}$$

where ${\sigma_0}^2$ and ${\sigma_r}^2$ are the variance of complete separation and complete mixing of particles, respectively. $\bar{c}$ and $\bar{n}$ are the average biomass particle concentration and the average number of particles in all sampling cells, respectively. c_i is the biomass particle concentration in cell *i*. *S* represents the deviation of the current particle mixing state. The lower and upper thresholds of MI are 0 and 1, respectively. MI = 0 indicates that different kinds of particles in the system are completely separated, while MI = 1 indicates that the system has reached a fully mixed state.

Fig. 9 shows the instantaneous particle mixing state and the time-evolution profiles of the particle mixing index. In the lower part of the BFB, biomass particles are mainly distributed in the area with high solid holdup and evenly distributed in the bed material, which shows good particle mixing efficiency. As shown in (b), after the initial start-up process, the particle mixing index reaches the dynamic equilibrium around the mean value of 0.8864, indicating a good particle mixing performance of the system.

In a dense gas–solid system, solid transportation performs an important effect on gas–solid characteristics (e.g., particle mixing, particle residence time) and the reactor performance. Solid transportation can be characterized by dispersion coefficient, which is defined for a single particle as follows [51]:

$$\mathrm{D_i} = \frac{(\Delta \mathrm{r_i})^2}{2\Delta \mathrm{t}} \tag{35}$$

where Δr_i denotes the displacement of particle *i* in time interval Δt. The average solid dispersion coefficient of the system is given by:

$$\mathrm{D} = \frac{1}{\mathrm{N_P}}\sum_{\mathrm{i}=1}^{\mathrm{N_P}}\frac{(\Delta \mathrm{r_i})^2}{2\Delta \mathrm{t}} \qquad (\mathrm{i} = 1, 2, \ldots, \mathrm{N_P}) \tag{36}$$

where N_p is the total number of particles in the system.

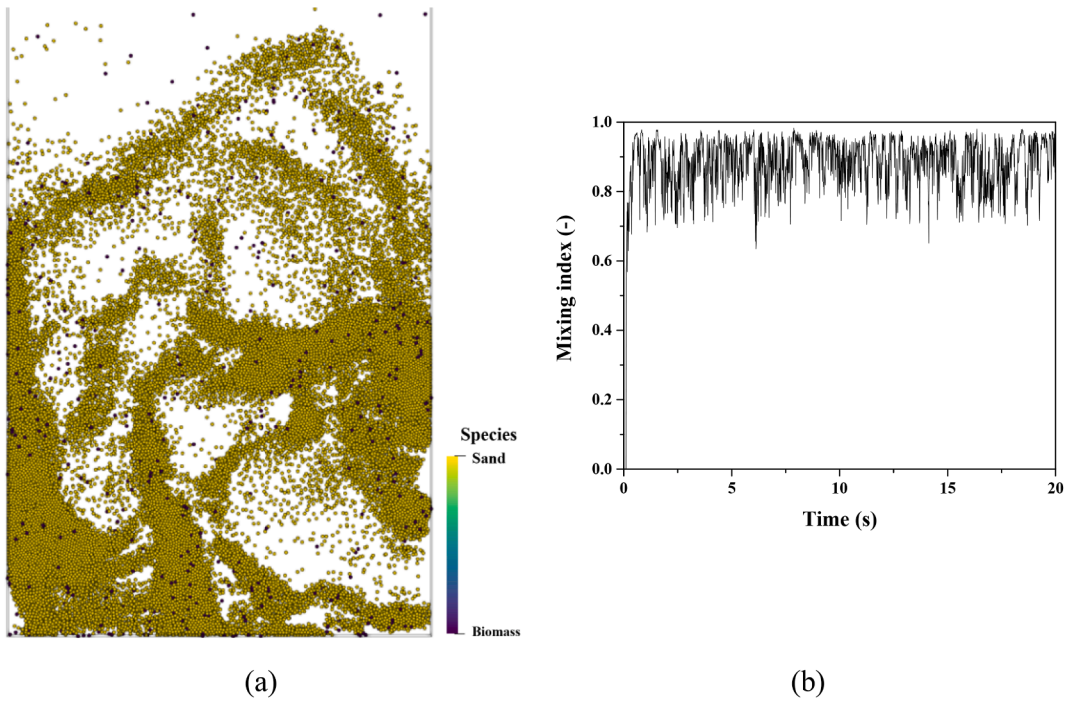

Fig. 9. Particle mixing in the BFB: (a) instantaneous particle mixing state; (b) variation of particle mixing index with time.

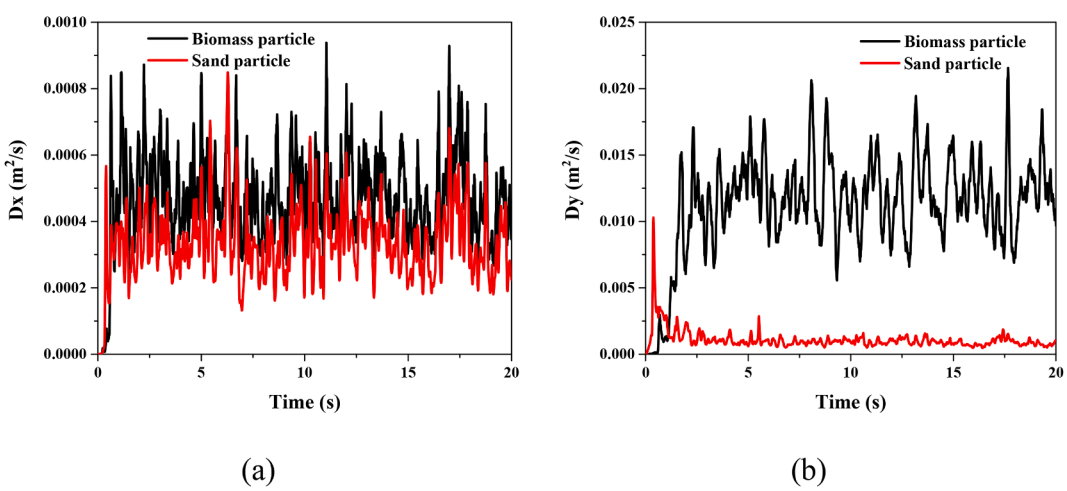

Fig. 10. Variation of solid dispersion coefficient with time: (a) horizontal direction (Dx); (b) vertical direction (Dy).

According to the previous studies, the solid dispersion coefficient in fluidized beds ranges from 0.0001 to 0.1 m^2/s [52,53]. As shown in Fig. 10(a), the solid horizontal dispersion coefficients of the two species are synchronous, but the solid horizontal dispersion coefficient of biomass particles is slightly larger than that of sand particles. After reaching the dynamic equilibrium state, the mean values of the horizontal dispersion coefficient of biomass particles and sand particles are 5.11×10^{-4} m^2/s and 3.82×10^{-4} m^2/s, respectively. Thus, the motions of these two kinds of particles in the horizontal direction are synchronous and governed by the bubble-emulsion phase interactions, and the motions of biomass particles are more intense due to their smaller density. As shown in Fig. 10(b), the solid vertical dispersion coefficient of sand particles has a peak value at the initial time, which corresponds to the initial start-up process. The solid vertical dispersion coefficients of sand and biomass particles in the dynamic equilibrium state are around the mean value of 9.7×10^{-4} m^2/s and 0.0127 m^2/s, respectively. The solid dispersion coefficient of sand particles in the vertical direction is almost three times that in the horizontal direction, and the solid dispersion coefficient of biomass particles in the vertical direction is two orders of magnitude larger than that in the horizontal direction, indicating that the introduced gas flow dominates the hydrodynamics in the BFB.

The evolution of solid dispersion coefficient and particle mixing index with temperature and S/B is given in Figs. 11 and 12, respectively. The solid dispersion coefficients of biomass and sand particles increase with the increase of operating temperature, and this phenomenon in the vertical direction is more obvious. According to the gas state equation ($PV = nRT$, P is gas pressure, V represents gas volume, n is gas molar quantity, R is the molar gas constant, T is gas temperature), the volume of gas expands as the operating temperature increases, which intensifies the particle motion. In addition, the increase of operating temperature promotes the heat and mass transfer in the BFB, resulting in the further decrease of the volume and mass of biomass particles. More gas products are then generated and the total gas volume increases. Therefore,

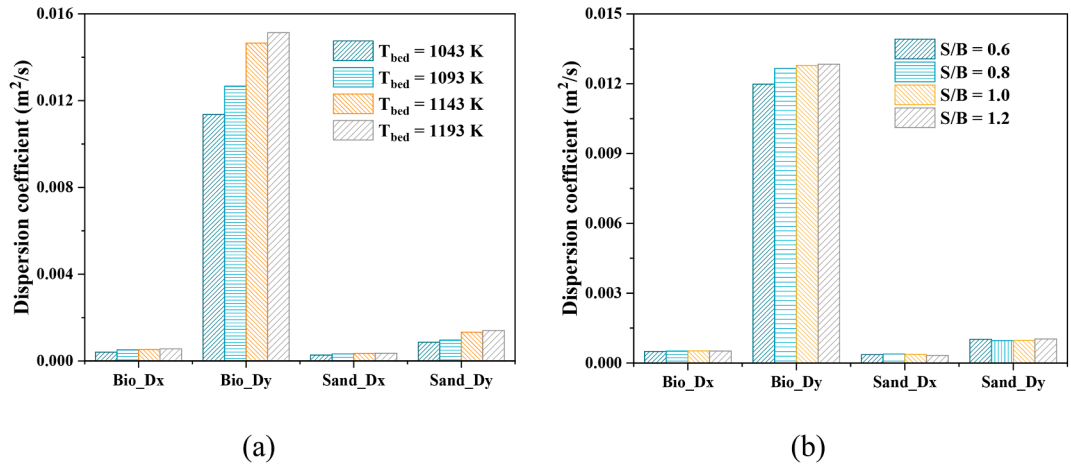

Fig. 11. Solid dispersion coefficients of sand and biomass particles under different operating temperatures (a) and S/B (b).

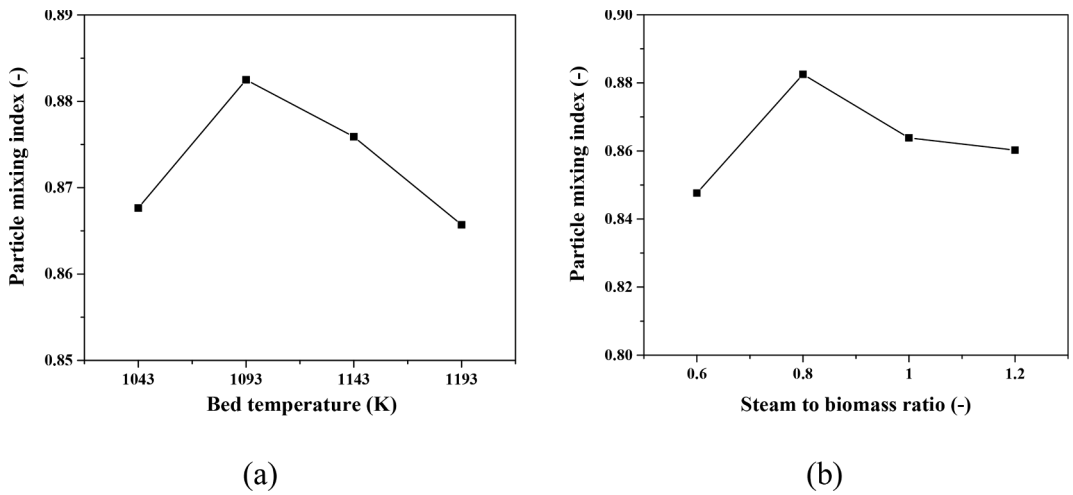

Fig. 12. Particle mixing index under different operating temperatures (a) and S/B (b).

increasing temperature performs a greater impact on the solid dispersion coefficient of biomass particles. The variation of S/B has little effect on the solid dispersion coefficient of sand particles. For biomass particles, the solid vertical dispersion coefficient is promoted under higher S/B, but the variation of the solid horizontal dispersion coefficient with S/B is not obvious. The increase of S/B leads to the increase of H_2O concentration in the BFB, which promotes the mass transfer process. The total gas volume increases and the volume and mass of biomass particles decrease, thus promoting the motion of biomass particles.

The increase of operating temperature and S/B first increases and then decreases the particle mixing index. The highest particle mixing index appears with the operating temperature in 1093 K and the S/B in 0.8. Increasing operating temperature and S/B intensifies the particle motion and the resulting mixing performance. Increasing operating temperature and S/B promotes the motions of biomass particles in the vertical direction. With the further increase of operating temperature and S/B, the motions of biomass particles in the vertical direction are more intense, and more biomass particles tend to move to the freeboard and escape from the reactor, leading to a decrease in particle mixing index.

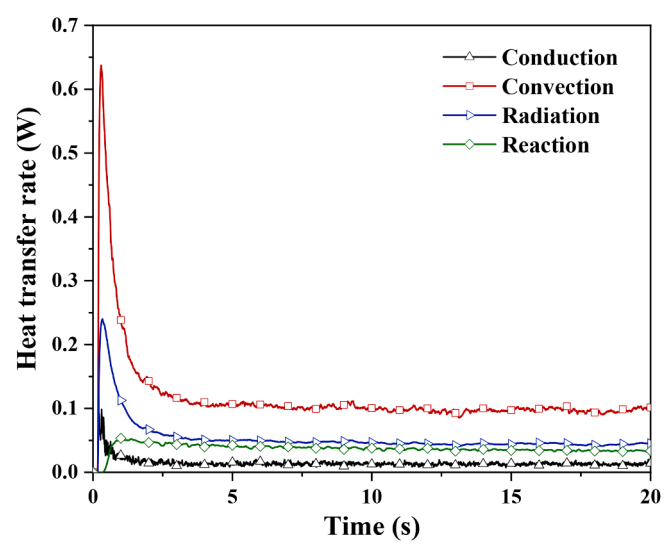

Fig. 13. Time-evolution profiles of the contribution of four heat transfer modes of biomass particles.

4.4. Heat transfer contribution

Good temperature control is the major advantage of the BFB, attributed to the excellent heat transfer performance. Specifically, heat

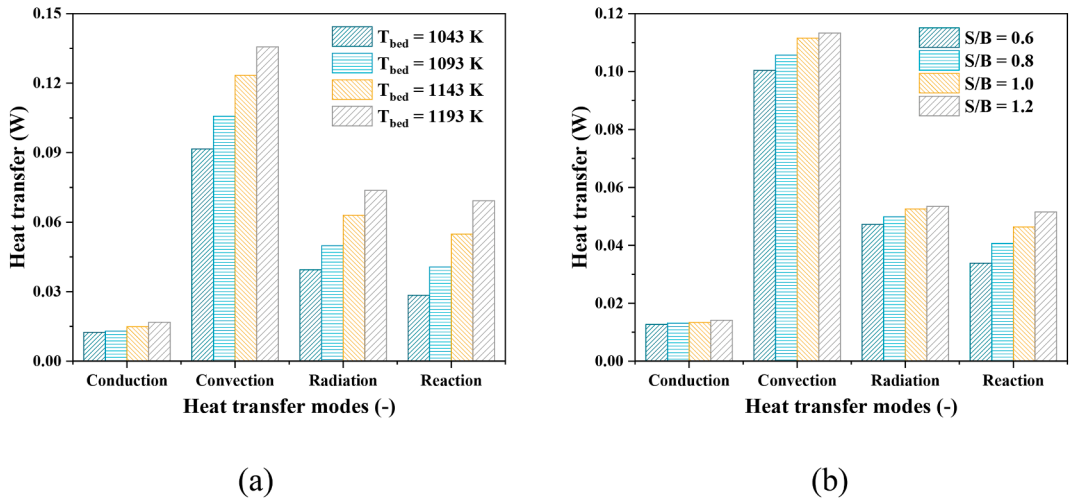

Fig. 14. Heat transfer contribution of different heat transfer modes under different operating temperatures (a) and S/B (b).

transfer affects chemical reaction rates and ultimately influences the quality of industrial products. Therefore, it is significant to study the heat transfer mechanism in the BFB. There are four heat transfer modes, including conduction, convection, radiation, and heat of reaction. At present, some studies were focused on the mechanism of heat transfer in fluidized beds with moderate operating conditions (e.g., low temperature, no radiation, and chemical reactions) [54–57], but the exploration of the heat transfer mechanism in the BFB during the biomass gasification has been seldom reported.

Fig. 13 gives the time-evolution profiles of the contribution of four heat transfer modes of biomass particles. At a specific time, the heat fluxes of all biomass particles in the BFB are averaged. At the initial time, the heat generated by conduction, convection, and radiation shows a peak value, and then decreases over time until the dynamic equilibrium state, while the start-up of the heat of reaction lags behind the other three heat transfer modes, which denotes that the low-temperature biomass particles experience a rapid heating process after entering the BFB, and the chemical reactions begin after reaching the required activation energy. After reaching the equilibrium state, the particle-averaged heat of conduction, convection, radiation, and reaction is 0.013 W, 0.106 W, 0.05 W, 0.041 W, respectively, and the particle-averaged heat of these four heat transfer modes accounts for 6.2%, 50.48%, 23.81%, 19.52% of the total heat, respectively. Therefore, in the heat transfer process occurring on biomass particles, convective heat transfer plays a dominant role, followed by radiative heat transfer and reactive heat transfer. The conductive heat transfer accounts for the

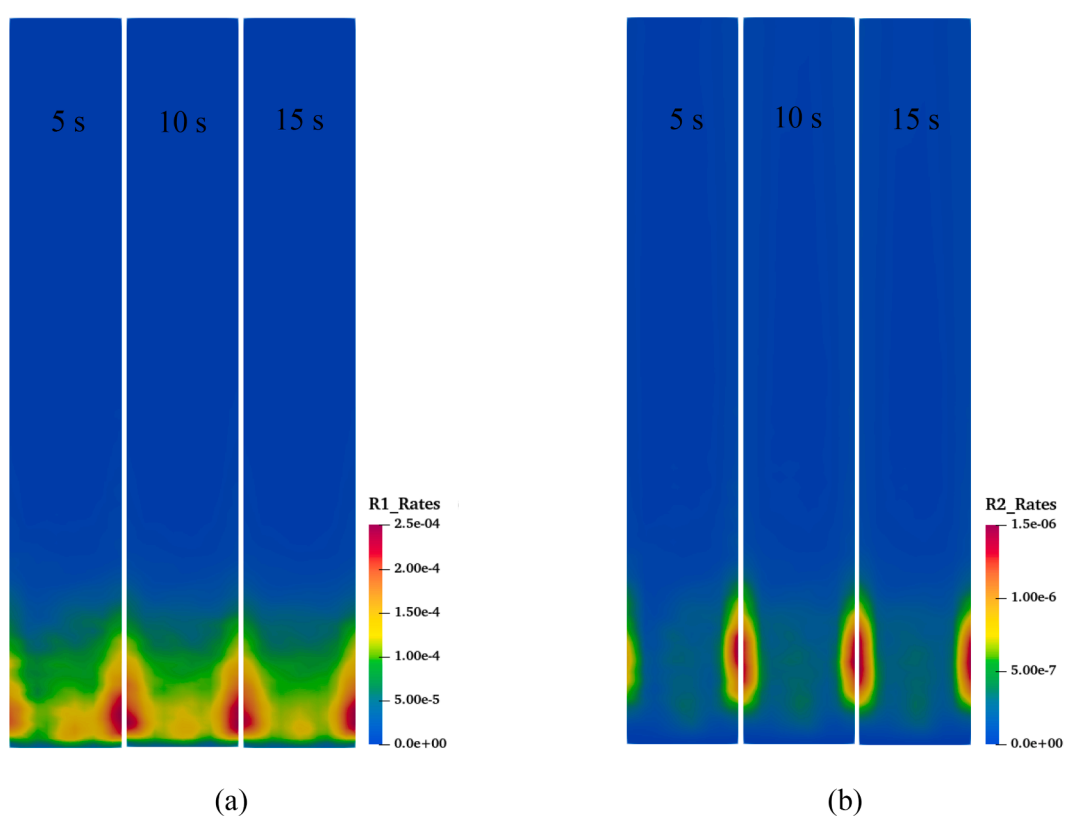

Fig. 15. Spatial distributions of reaction rates in the central slice of the BFB at different times: (a) R1; (b) R2; (c) R3; (d) R4; (e) pyrolysis.

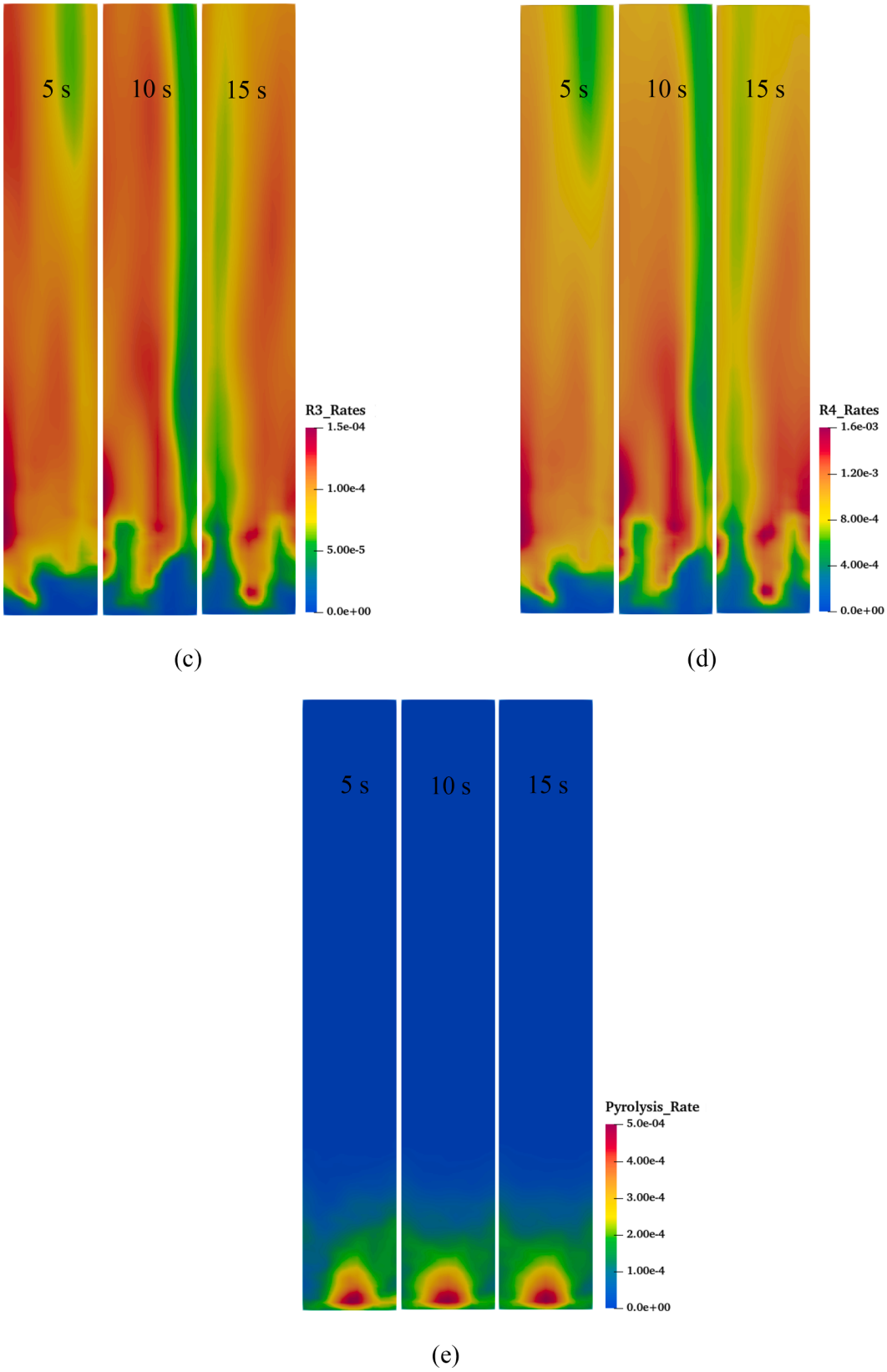

Fig. 15. (*continued*).

smallest proportion. In the BFB, the conductive heat transfer takes place during particle collisions. The collision of particles is random and discontinuous, which leads to the fact that the conductive heat transfer mode cannot occur on all particles in the system at the same time, and the total heat generated by conductive heat transfer mode is the smallest among all heat transfer modes.

Fig. 14 illustrates the heat transfer contribution of different heat transfer modes under different operating temperatures and S/B. With

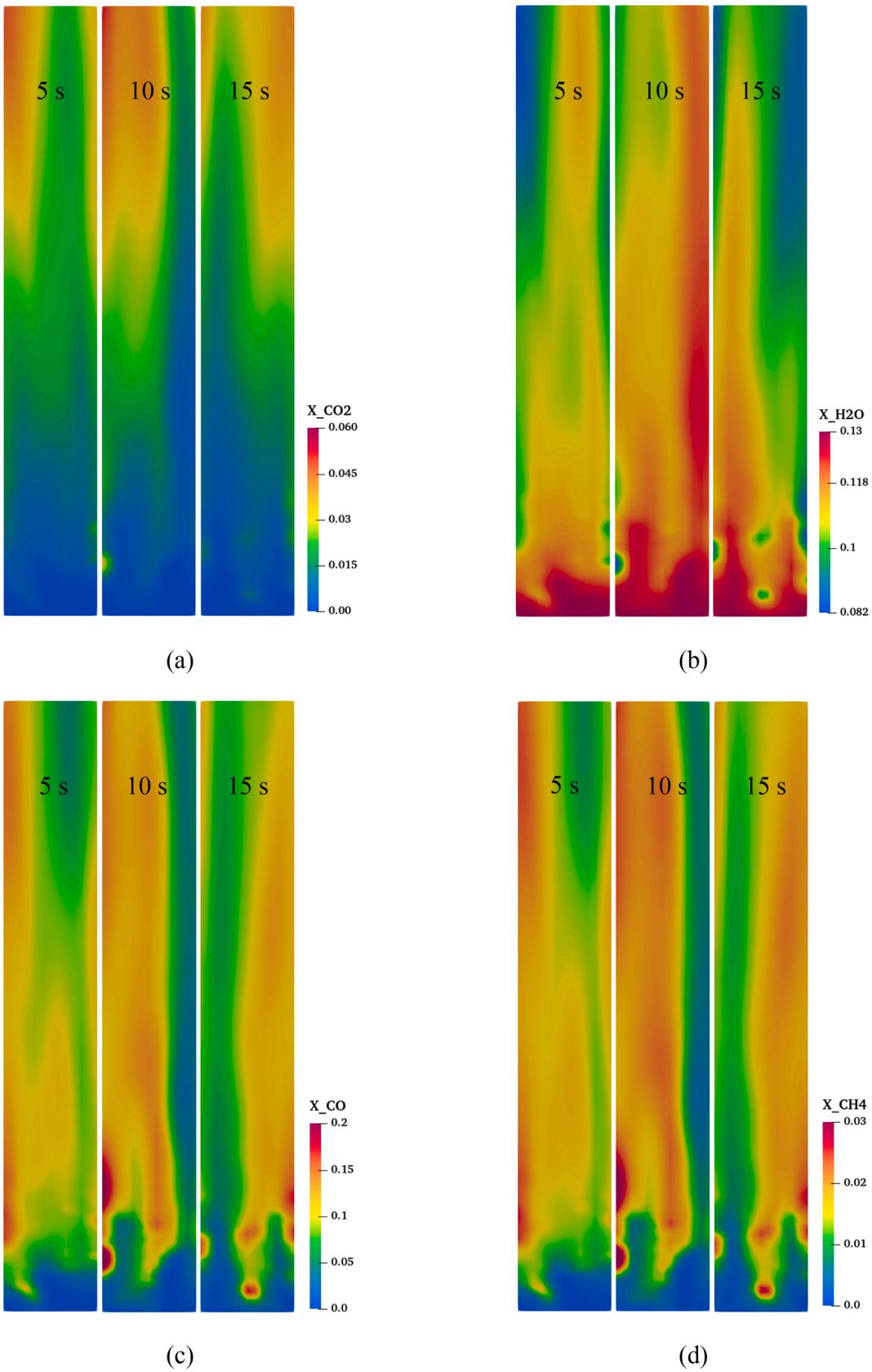

Fig. 16. Spatial distributions of gas species in the central slice of the BFB at different times: (a) CO_2; (b) H_2O; (c) CO; (d) CH_4; (e) H_2.

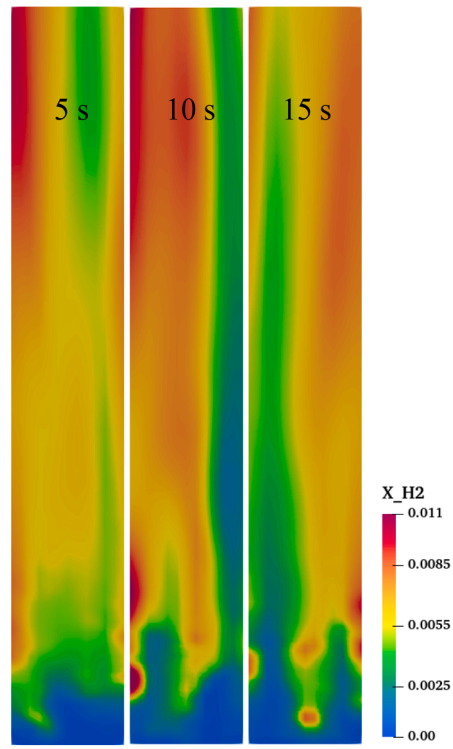

(e)

Fig. 16. (*continued*).

the increase of operating temperature, the larger temperature difference between biomass particles and gas/sand particles leads to more intense heat transfer, and the increased heat generated by conductive, convective, and radiative heat transfer. Higher temperature promotes endothermic reactions and increases the heat consumed by reactions. Increasing S/B increases the heat generated by four heat transfer modes. Larger S/B leads to an increase of H_2O and promotes the gasification reactions (i.e., R1, R3, and R4), and thus more heat is consumed during the reaction process. Therefore, with the increase of S/B, the biomass temperature decreases and the temperature difference between biomass particles and operating temperature increases, which leads to an increase of heat generated through conductive, convective, and radiative heat transfer modes.

4.5. Reaction rates and gas species

The distribution of reaction rates (kmol/s) and gas species in the central slice of the BFB at different time instants are given in Figs. 15 and 16. The reaction rates and gas species distributions are slightly different at different time instants, but the distribution trend is roughly the same. After entering the BFB, the pyrolysis process rapidly occurs at high temperatures in the dense region, corresponding to the high pyrolysis rate (see Fig. 15(e)). Moreover, the pyrolysis rate in the middle of the dense region is much higher than that in the near-wall region. In the bottom region, particles tend to move towards the middle region (see Figs. 5 and 6), and the accumulation of biomass particles results in a higher pyrolysis rate in this region. In the freeboard, the pyrolysis rate is

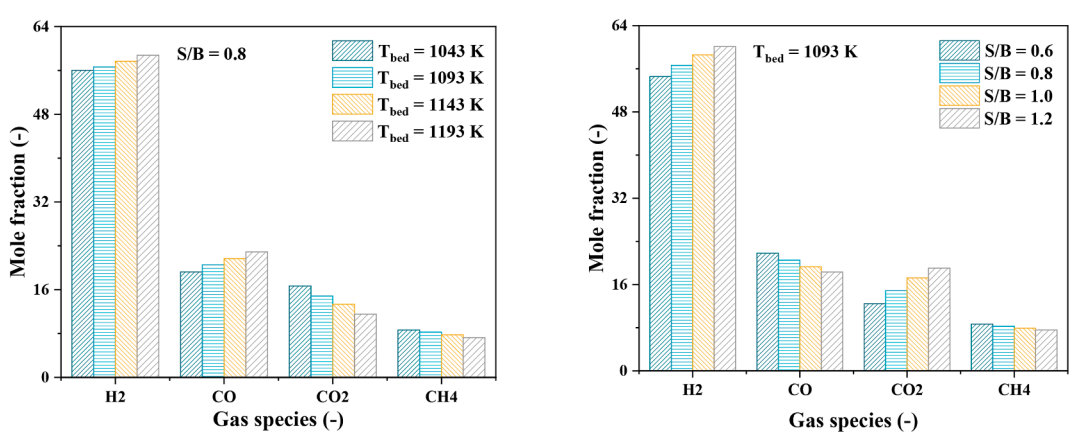

(a) (b)

Fig. 17. Mole fraction of gas species with different operating temperatures (a) and S/B (b) at the BFB outlet.

almost zero, indicating that the biomass pyrolysis process is completed in the dense region. The distribution of heterogeneous reaction rates is quite different from that of homogeneous reaction rates. The heterogeneous reactions (e.g., R1, R2) mainly occur in the dense region of the BFB, and the reaction rate is higher in the near-wall region, indicating a higher char concentration here. The distribution of homogeneous reaction rates is consistent with the distribution of reactant gas species (e.g., CO, CH_4). There is a high homogeneous reaction rate near the bed surface, indicating that the homogeneous reactions mainly occur in this region, which is in accordance with that of the results as reported in previous studies [15]. High gas concentration corresponds to high homogeneous reaction rates. CH_4, CO, and H_2 are mainly produced from the pyrolysis process, and the distributions of these three gas species are roughly the same. CO_2 is mainly distributed in the upper part of the BFB, and the distribution trend is opposite to that of H_2O, indicating that CO_2 mainly comes from the water–gas shift reaction.

Fig. 17 gives the gas species at the BFB outlet at different operating parameters. With the increase of operating temperature, the concentration of H_2 and CO increases while the concentration of CO_2 and CH_4 decreases. Increasing operating temperature promotes reaction rates due to the endothermic reaction in the biomass gasification process. Specifically, for the reversible reaction (i.e., R4), increasing operating temperature promotes the positive reaction. Further progress of reactions R1, R3, and R4 at higher temperatures results in an increase of H_2 and a decrease of CH_4. The promotion of char conversion by higher temperature leads to an increase in CO_2 consumption and CO production. With the increase of S/B, the concentration of H_2O in the BFB increases, which promotes gasification reactions R1 and R3, and reaction R4 is promoted in the positive direction. Therefore, the consumption of CO and CH_4 and the production of CO_2 and H_2 increase. The effects of operating temperature and S/B on the gasification products are in line with the CFD-DEM simulation results reported in previous literature [25].

5. Conclusion

In this study, the particle behaviours during the biomass gasification process in a quasi-3D BFB reactor are numerically studied based on a CFD-DEM approach featuring thermochemical and polydispersity effects. Particle motions, particle mixing, solid dispersion and heat transfer contribution of different heat transfer modes are comprehensively explored. The effects of operating parameters on particle behaviours are unveiled. Conclusions are drawn as follows:

1) Bubble dynamics plays a crucial role in shaping flow patterns. At the bottom, particles tend to move to the middle region and then be carried upward by bubbles. Particles move upwards with the bubble until it bursts, and then are scattered in the freeboard. The typical particle behaviours improve the mixing performance and the resulting heat and mass transfer.
2) The motions of sand and biomass particles in the horizontal direction are synchronous. The solid vertical dispersion coefficient of biomass particles is much higher than that of sand particles due to the smaller mass and size of biomass particles. Moreover, the solid vertical dispersion coefficients are much higher than the solid horizontal dispersion coefficients, indicating that the introduced gas flow dominates bed hydrodynamics. The solid dispersion coefficients of biomass and sand particles are enhanced under higher temperatures, and the increase of S/B promotes the solid vertical dispersion coefficient of biomass particles. The particle mixing index first increases and then decreases with the increase of operating temperature and S/B.
3) The start-up of reactive heat transfer lags behind the other three heat transfer modes. In the heat transfer process occurring on biomass particles, convective heat transfer plays a dominant role, followed by radiative heat transfer and reactive heat transfer. Conductive heat transfer accounts for the smallest proportion. Increasing operating temperature and S/B promotes the conductive, convective, radiative and reactive heat transfer.
4) After entering the reactor, the biomass particles are carried by the particles in the bottom and move to the middle region, where the pyrolysis reaction takes place. Therefore, the middle part of the dense region has the highest biomass pyrolysis reaction rate. The heterogeneous reactions mainly occur in the dense region of the bed, and the reaction rate is higher in the near wall region, indicating a higher char concentration here. The distribution of homogeneous reaction rates is consistent with that of the main gas species concentration.

Declaration of Competing Interest

The authors declare that they have no known competing financial interests or personal relationships that could have appeared to influence the work reported in this paper.

Acknowledgments

This work is supported by National Science Fund for Distinguished Young Scholars (No. 51925603), National Key Research and Development Plan of China (Nos. 2017YFB0601805, 2017YFE0112500) and the National Natural Science Foundation of China (No. 51806192), to which we are grateful.

Appendix A. Supplementary data

Supplementary data to this article can be found online at https://doi.org/10.1016/j.cej.2021.131847.

References

[1] D. Kong, S. Wang, K. Luo, C. Hu, D. Li, J. Fan, Three-dimensional simulation of biomass gasification in a full-loop pilot-scale dual fluidized bed with complex geometric structure, Renew. Energy 157 (2020) 466–481.
[2] S. Wang, Y. Shen, CFD-DEM study of biomass gasification in a fluidized bed reactor: effects of key operating parameters, Renew. Energy 159 (2020) 1146–1164.
[3] S. Tao, J. Wu, L. Shen, J. Xiao, Experimental investigation on hydrogen production from biomass gasification in interconnected fluidized beds, Biomass Bioenergy 36 (2012) 258–267.
[4] S. Kern, C. Pfeifer, H. Hofbauer, Gasification of wood in a dual fluidized bed gasifier: influence of fuel feeding on process performance, Chem. Eng. Sci. 90 (2013) 284–298.
[5] T. Li, J.F. Dietiker, L. Shadle, Comparison of full-loop and riser-only simulations for a pilot-scale circulating fluidized bed riser, Chem. Eng. Sci. 120 (2014) 10–21.
[6] S. Wang, Y. Shen, Particle-scale study of heat and mass transfer in a bubbling fluidised bed, Chem. Eng. Sci. 240 (2021) 116655, https://doi.org/10.1016/j.ces.2021.116655.
[7] Y. Cheng, Z. Thow, C. Wang, Biomass gasification with CO2 in a fluidized bed, Powder Technol. 296 (2016) 87–101.
[8] A. Klimanek, J. Bigda, CFD modelling of CO2 enhanced gasification of coal in a pressurized circulating fluidized bed reactor, Energy 160 (2018) 710–719.
[9] T.M. Ismail, M. Abd El-Salam, E. Monteiro, A. Rouboa, Eulerian-Eulerian CFD model on fluidized bed gasifier using coffee husks as fuel, Appl. Therm. Eng. 106 (2016) 1391–1402.
[10] J. Wang, Continuum theory for dense gas-solid flow: a state-of-the-art review, Chem. Eng. Sci. 215 (2020) 115428, https://doi.org/10.1016/j.ces.2019.115428.
[11] S. Yang, H. Wang, Y. Wei, J. Hu, J.W. Chew, Particle-scale modeling of biomass gasification in the three-dimensional bubbling fluidized bed, Energy Convers. Manage. 196 (2019) 1–17.
[12] I.S. Hwang, J. Sohn, U.D. Lee, J. Hwang, CFD-DEM simulation of air-blown gasification of biomass in a bubbling fluidized bed gasifier: effects of equivalence ratio and fluidization number, Energy 219 (2021), 119533.
[13] C. Li, Q. Eri, Comparison between two eulerian-lagrangian methods: CFD-DEM and MPPIC on the biomass gasification in a fluidized bed, Biomass Convers. Biorefin. 11 (2021) 1–18.
[14] S. Yang, H. Wang, Y. Wei, J. Hu, J.W. Chew, Eulerian-lagrangian simulation of air-steam biomass gasification in a three-dimensional bubbling fluidized gasifier, Energy 181 (2019) 1075–1093.
[15] S. Wang, K. Luo, C. Hu, L. Sun, J. Fan, Impact of operating parameters on biomass gasification in a fluidized bed reactor: an Eulerian-Lagrangian approach, Powder Technol. 333 (2018) 304–316.

[16] X. Ku, H. Jin, J. Lin, Comparison of gasification performances between raw and torrefied biomasses in an air-blown fluidized-bed gasifier, Chem. Eng. Sci. 168 (2017) 235–249.
[17] P. Ostermeier, F. Fischer, S. Fendt, S. Deyoung, H. Spliethoff, Coarse-grained CFD-DEM simulation of biomass gasification in a fluidized bed reactor, Fuel 255 (2019) 115790–115791.
[18] S. Wang, K. Luo, J. Fan, CFD-DEM coupled with thermochemical sub-models for biomass gasification: validation and sensitivity analysis, Chem. Eng. Sci. 217 (2020), 115550.
[19] D. Liu, X. Chen, Experimental profiles of lateral mixing of feed particles in a three-dimensional fluidized bed, AIChE J. 57 (2011) 1459–1469.
[20] E. Michaelides, C.T. Crowe, J.D. Schwarzkopf, Multiphase Flow Handbook, CRC Press, 2016.
[21] P.A. Cundall, O.D. Strack, A discrete numerical model for granular assemblies, Geotechnique 29 (1979) 47–65.
[22] Y. Tsuji, T. Kawaguchi, T. Tanaka, Discrete particle simulation of two-dimensional fluidized bed, Powder Technol. 77 (1993) 79–87.
[23] R. Garg, J. Galvin, T. Li, S. Pannala, Open-source MFIX-DEM software for gas–solids flows: part I—Verification studies, Powder Technol. 220 (2012) 122–137.
[24] G.K. Batchelor, and R.W. O'Brien, Thermal or electrical conduction through a granular material. Proceedings of the Royal Society of London. A. Mathematical and Physical Sciences 355 (1977) 313-333.
[25] X. Ku, T. Li, T. Løvås, CFD–DEM simulation of biomass gasification with steam in a fluidized bed reactor, Chem. Eng. Sci. 122 (2015) 270–283.
[26] J. Bruchmüller, B.G.M. Van Wachem, S. Gu, K.H. Luo, R.C. Brown, Modeling the thermochemical degradation of biomass inside a fast pyrolysis fluidized bed reactor, AIChE J. 58 (2012) 3030–3042.
[27] R.J. Hill, D.L. Koch, A.J. Ladd, Moderate-Reynolds-number flows in ordered and random arrays of spheres, J. Fluid Mech. 448 (2001) 243.
[28] D. Gidaspow, Multiphase Flow and Fluidization: Continuum and Kinetic Theory Descriptions, Academic press, 1994.
[29] R. Beetstra, M.A. van der Hoef, J. Kuipers, Drag force of intermediate Reynolds number flow past mono-and bidisperse arrays of spheres, AIChE J. 53 (2007) 489–501.
[30] R. Beetstra, M. Hoef, J. Kuipers, Numerical study of segregation using a new drag force correlation for polydisperse systems derived from lattice-Boltzmann simulations, Chem. Eng. Sci. 62 (2007) 246–255.
[31] H. Liu, R.J. Cattolica, R. Seiser, C. Liao, Three-dimensional full-loop simulation of a dual fluidized-bed biomass gasifier, Appl. Energy 160 (2015) 489–501.
[32] N. Prakash, T. Karunanithi, Kinetic modeling in biomass pyrolysis – a review, J. Appl. Sci.Res. 4 (2008) 1627–1636.
[33] J. Mabrouki, M.A. Abassi, K. Guedri, A. Omri, M. Jeguirim, Kinetic and characteristic studies on the pyrolysis of vine stems, almond shell and Ziziphus wood using thermo-gravimetric analysis (TGA), Int. Renew.Energy Congress (IREC) (2016).
[34] N. Abani, A.F. Ghoniem, Large eddy simulations of coal gasification in an entrained flow gasifier, Fuel 104 (2013) 664–680.
[35] W.P. Jones, R.P. Lindstedt, Global reaction schemes for hydrocarbon combustion, Combust. Flame 73 (1988) 233–249.
[36] A. Gómez-Barea, B. Leckner, Modeling of biomass gasification in fluidized bed, Prog. Energ. Combust. 36 (4) (2010) 444–509.
[37] F. Bustamante, R.M. Enick, R.P. Killmeyer, B.H. Howard, M.V. Ciocco, Uncatalyzed and wall-catalyzed forward water–gas shift reaction kinetics, AIChE J. 51 (2010) 1440–1454.
[38] D.A. Clarke, A.J. Sederman, L.F. Gladden, D.J. Holland, Investigation of void fraction schemes for use with CFD-DEM simulations of fluidized beds, Ind. Eng. Chem. Res. 57 (2018) 3002–3013.
[39] J. Cardoso, V. Silva, D. Eusebio, P. Brito, R.M. Boloy, L. Tarelho, J.L. Silveira, Comparative 2D and 3D analysis on the hydrodynamics behaviour during biomass gasification in a pilot-scale fluidized bed reactor, Renew. Energy 131 (2018) 713–729.
[40] J. Lin, K. Luo, L. Sun, S. Wang, C. Hu, J. Fan, Numerical investigation of nickel-copper oxygen carriers in chemical-looping combustion process with zero emission of CO and H2, Energy Fuel. 33 (2019) 12096–12105.
[41] F. Song, F. Li, W. Wang, J. Li, A sub-grid EMMS drag for multiphase particle-in-cell simulation of fluidization, Powder Technol. 327 (2018) 420–429.
[42] R.B. Bird, Transport phenomena, Appl. Mech. Rev. 55 (2002) R1–R4.
[43] A. Burcat, and B. Ruscic, Third millenium ideal gas and condensed phase thermochemical database for combustion (with update from active thermochemical tables)., Argonne National Lab.(ANL), Argonne, IL (United States), 2005.
[44] C. Loha, H. Chattopadhyay, P.K. Chatterjee, Three dimensional kinetic modeling of fluidized bed biomass gasification, Chem. Eng. Sci. 109 (2014) 53–64.
[45] S. Wang, K. Luo, C. Hu, J. Lin, J. Fan, CFD-DEM simulation of heat transfer in fluidized beds: model verification, validation, and application, Chem. Eng. Sci. 197 (2019) 280–295.
[46] S. Wang, K. Luo, S. Yang, C. Hu, J. Fan, Parallel LES-DEM simulation of dense flows in fluidized beds, Appl. Therm. Eng. 111 (2017) 1523–1535.
[47] A.V. Patil, E. Peters, J. Kuipers, Comparison of CFD–DEM heat transfer simulations with infrared/visual measurements, Chem. Eng. J. 277 (2015) 388–401.
[48] W. Yin, S. Wang, K. Zhang, Y. He, Investigation of oxygen-enriched biomass gasification with TFM-DEM hybrid model, Chem. Eng. Sci. 211 (2019), 115293.
[49] C. Hu, K. Luo, M. Zhou, J. Lin, D. Kong, J. Fan, Influences of secondary gas injection pattern on fluidized bed combustion process: A CFD-DEM study, Fuel 268 (2020), 117314.
[50] P.M.C. Lacey, Developments in the theory of particle mixing, J. Appl. Chem. 4 (1954) 257–268.
[51] D. Liu, R. Chen, Lateral solids dispersion coefficient in large-scale fluidized beds, Combust. Flame 157 (2010) 2116–2124.
[52] R.W. Breault, A review of gas–solid dispersion and mass transfer coefficient correlations in circulating fluidized beds, Powder Technol. 163 (2006) 9–17.
[53] J. Sánchez-Prieto, F. Hernández-Jiménez, L.M. Garcia-Gutierrez, A. Soria-Verdugo, Experimental study on the characteristic mixing time of solids and its link with the lateral dispersion coefficient in bubbling fluidized beds, Chem. Eng. J. 307 (2017) 113–121.
[54] K. Zhang, S. Wang, B. Li, Y. He, Y. Zhao, Heat transfer in a pulsed fluidized bed by using coupled CFD-DEM method, Powder Technol. 367 (2020) 497–505.
[55] L. Lu, A. Morris, T. Li, S. Benyahia, Extension of a coarse grained particle method to simulate heat transfer in fluidized beds, Int. J. Heat Mass Transf. 111 (2017) 723–735.
[56] Y. Zhao, M. Jiang, Y. Liu, J. Zheng, Particle-scale simulation of the flow and heat transfer behaviors in fluidized bed with immersed tube, AIChE J. 55 (2010) 3109–3124.
[57] Z. Zhou, A.B. Yu, P. Zulli, Particle scale study of heat transfer in packed and bubbling fluidized beds, AIChE J. 55 (2009) 868–884.